ARTICLE   OPEN

Check for updates

Design of refractory multi-principal-element alloys for high-temperature applications

Gaoyuan Ouyang [1 ✉], Prashant Singh[1], Ranran Su[2], Duane D. Johnson [1,3 ✉], Matthew J. Kramer [1], John H. Perepezko[2], Oleg N. Senkov[4], Daniel Miracle[4] and Jun Cui[1,3 ✉]

Refractory multi-principal-element alloys (RMPEAs) exhibit high specific strength at elevated temperatures (T). However, current RMPEAs lack a balance of room-temperature (RT) ductility, high-T strength, and high-T creep resistance. Using density-functional theory methods, we scanned composition space using four criteria: (1) formation energies for operational stability: $-150 \leq E_f \leq +70$ meV per atom; (2) higher strength found via interstitial electron density with Young's moduli $E > 250$ GPa; (3) inverse Pugh ratio for ductility: $G/B < 0.57$; and (4) high melting points: $T_m > 2500\,°C$. Using rapid bulk alloy synthesis and characterization, we validated theory and down-selected promising alloy compositions and discovered $Mo_{72.3}W_{12.8}Ta_{10.0}Ti_{2.5}Zr_{2.5}$ having well-balanced RT and high-T mechanical properties. This alloy has comparable high-T compressive strength to well-known MoNbTaW but is more ductile and more creep resistant. It is also superior to a commercial Mo-based refractory alloy and a nickel-based superalloy (Haynes-282) with improved high-T tensile strength and creep resistance.

INTRODUCTION

As the world pursues carbon-neutral power generation, the gas turbine is expected to play a vital role. Modern gas turbines can burn hydrogen, which can be produced, amongst other methods, via water electrolysis using wind power during off-peak hours[1,2]. Hydrogen burns hotter than natural gas[3], which makes gas turbines more efficient assuming operational temperatures can be pushed higher without damaging the turbine blades. The current generation high-speed blade materials are Ni-based superalloys with melting points near 1350 °C, reduced below 1250 °C at the zone between the bond coat and single-crystal blade. They are operated at 1100 °C and require thermal-barrier coatings and internal cooling to withstand the working gas as hot as 1600 °C[4,5]. A next-generation material that can operate at/above 1300 °C, remain phase stable while retaining strength, and permit the use of hotter gas (while reducing the need for internal cooling) will improve fuel efficiency by as much as 7% and reduce environmental-damaging emissions[6].

Refractory multi-principal-element alloys (RMPEA) are promising alloys for high-temperature (HT) applications[7] if stability, strength, and oxidation resistance in harsh-service conditions can be addressed. Using only the high-entropy alloy concept presupposes that higher configurational (mixing) entropy S_{conf} that competes with formation energy E_f [not too positive (clustering) or too negative (strongly ordering)] and lattice strain lead to higher stability and strength[8,9]. The high entropy alloy (HEA) concept[10] has resulted in a class of materials that promise improved strength or toughness[11–13], especially at cryogenic temperatures[8,14–18], and corrosion properties[19–23]. High entropy was identified for higher phase stability in the earlier studies, but a more careful consideration shows it is not a major factor[24]. Notably, with more alloying elements, N, introduces the more likely possibility (e.g., from electronegativity differences) that at least one pair of $\frac{1}{2}N(N-1)$ pairs will be strongly ordered, so

alloying effects and chemistry, i.e., non-equiatomic compositions, remain very important. Ideally, RMPEAs are single-phase systems with extremely high melting points, and high specific strength via solid-solution strengthening well above 1000 °C. The first two RMPEAs reported with HT strength well above other metal alloys are equiatomic solid-solutions MoNbTaW and MoNbTaVW[9,25]. They offer exceptional compressive yield strength of 400–700 MPa at 1600 °C, whereas in typical Ni-based superalloys, e.g., Inconel 718, yield strength drops to near zero near 1200 °C[8]. Such a significant difference in mechanical strength at high temperatures testifies to the potential of RMPEAs. Unfortunately, these two RMPEAs are brittle at room temperature (RT). Efforts were made to improve their ductility, but always resulted in a significant loss of HT strength. For example, the equiatomic HfNbTaTiZr alloy exhibits good RT ductility, up to 50% deformation can be reached under compression[26], but the HT yield strength is low, only 92 MPa at 1200 °C[27]. Another alloy that is promising is HfMoNbTaTi alloy, which shows 27% RT compressive strain. Its compressive yield strength maintained at 699 MPa at 1200 °C then dropped to 367 MPa at 1400 °C[28]. When constrained by high configurational entropy (i.e., $N > 4$ with equiatomic composition), finding an RMPEA viable for HT application is quickly limited. Fortunately, numerous non-equiatomic RMPEAs do indeed retain single-phase solid solutions (and multiphase for strengthening, controlled by composition) that exhibit superior mechanical properties (e.g. refs. [8,29,30]). By removing the equiatomic constraint, the MPEA composition space expands significantly yet demands an excessive amount of computational and experimental work. The high-throughput (HTP) scheme is one such approach[31–41] which, when combined with numerically efficient density-functional theory (DFT) methods[42], can enable accurate MPEA design[29]. Experimentally, methods like rapid alloy prototyping[31], diffusion-multiples[32], additive manufacturing[43,44], and thin-film-related co-deposition[33,45] have been successful. Recently,

[1]Division of Materials Science and Engineering, Ames Laboratory, Ames, IA 50011, USA. [2]Department of Materials Science and Engineering, University of Wisconsin-Madison, Madison, WI 53706, USA. [3]Department of Materials Science and Engineering, Iowa State University, Ames, IA 50011, USA. [4]Air Force Research Laboratory, Materials and Manufacturing Directorate, Wright-Patterson Air Force Base, Dayton, OH 45433, USA. ✉email: gaoyuan@iastate.edu; ddj@iastate.edu; cuijun@iastate.edu

npj

computation materials science has started to play a critical role in HEA development, including works like CALPHAD-based high-throughput computational method[24,34], machine learning assisted design coupled with modeling/experimental data[35,36,46], and density functional theory (DFT) method[37]. However, past effort focused on either computation or experiments with a limited synergy of the two. Moreover, there has been limited or no focus on developing numerically efficient ways to directly use DFT in MPEA design.

Here, based on our recent success[42], we developed a numerically efficient screening strategy combining HTP-DFT with experimental validation along with high-fidelity testing (RT and HT) for efficiently exploring the vast RMPEA compositional space. The strategy focuses on assessing and down-selecting worthwhile alloys under a chosen set of constraints: (Tier 1) HTP-DFT calculations (with specific metrics) are used; (Tier 2) secondary down-selection from exhaustive DFT results are then validated and additionally screened by rapid bulk-alloy synthesis and characterization at RT (modulus); and (Tier 3) small-sample punch tests are performed at high temperatures for creep and tensile mechanical properties. By applying Tier 2 and 3 screening, this strategy led us to the discovery of a Mo-rich RMPEA with well-balanced mechanical properties within 12 months.

RESULTS AND DISCUSSION
Alloy design and screening
Tier 1 screening and down-selection employed the well-established, DFT-based Korringa–Kohn–Rostoker coherent potential approximation (KKR-CPA) calculations to average directly all possible alloy configurations and to predict the relative structural phase stability (i.e., formation energy, E_f; Fig. 1a), structural parameters (lattice constants, $\{a_i\}$), and bulk moduli (B; Fig. 1b) for the entire design space, i.e., for any arbitrary composition solid-solution[29,47–50]. Importantly, recently we have shown that the interstitial electron density ρ_o (obtained directly by KKR-CPA) provides a universal metric r_s for maximum strength[42] for any metal (elemental, crystalline, or amorphous); r_s (Fig. 1c) is a DFT exchange-correlation parameter (with $\rho_o = \frac{4\pi}{3}r_s^3$) for a homogeneous electron gas—which exhibits universal behavior for all elastic moduli and shear strength. As r_s involves only interstitial electrons (independent of any alloying element), a rule-of-mixtures (RoM) r_s^{RoM} is valid and, notably, provides a reliable a priori estimate of relative strength, as we have already verified[42] (i.e., r_s^{RoM} down-selected regions agree with direct KKR-CPA results as we verified experimentally in a subset of alloys). Hence, r_s^{RoM} for any RMPEA composition directly narrows the search ranges (Fig. 1c) for alloys with the highest strength criterion (largest r_s^{RoM}'s—with r_s post-verified by KKR-CPA). Subsequently, those alloys with the most stable criterion (E_f from KKR-CPA) were down-selected for single-phase (bcc) stability. The smaller the r_s the higher the strength, where the smallest r_s for elemental metals is 1.5 as found for Iridium[42]. From the four criteria, r_s and formation energy E_f can show competing behavior, for example, the alloy is more brittle if r_s indicates higher strength but E_f is too negative (too stable or too strongly bonded), as is verified by the ductility criteria, as discussed in results. Notably, the high-strength alloys down-selected and characterized here were the same as given initially by r_s^{RoM}.

For the five-element MoWTaTiZr system, we directly evaluated 8000 compositions using KKR-CPA with Mo, W, and Ta varied at 5 at.% intervals and with Ti:Zr ratio fixed at 1:1 (see ref. [29], small amounts of Ti:Zr provide an electron-dispersion effect to stabilize the alloy). To expedite the down-selection of compositions with $-150 \leq E_f \leq +70$ meV and bulk moduli $B > 200$ GPa, we used alloy lattice constants estimated by Vegard's rule[51] (i.e., $\bar{a} \approx \sum_{i=1}^{N} c_i a_i^o$, with compositions $\{c_i\}$ and a_i^o are the optimized elemental lattice constants); down-selected alloy composition was then fully optimized as needed. The E_f criteria arise[29] from the observation that complex phases (e.g., sigma phase) form when $E_f > +70$ meV and metastable metallic glasses form or ordered phases appear when $E_f < -150$ meV[52]. The alloys that met the E_f, r_s, B_0, and Pugh's ratio for ductility criteria are depicted in Fig. 1. A further screening was conducted based on forming a solid solution using the Hume-Rothery rules, which describe that solute and host atoms must be similar in electronegativities, crystal structure, atomic radii (difference < 15%), and valence-electron concentration (4 < VEC < 6). The compositions that satisfied the Hume–Rothery rules were examined by calculating the Warren-Cowley short-range order parameters using KKR-CPA linear response, which predicts (if the alloy forms a disordered solid solution) what low-T ordering or spinodal decomposition is expected[53]. The Tier 1 screening generated four compositions of interest: $(MoW)_{80}Ta_{12.5}(TiZr)_{7.5}$, $(MoW)_{80}Ta_{10}(TiZr)_{10}$, $(MoW)_{80}Ta_{20}(TiZr)_0$, and $(MoW)_{85}Ta_{10}(TiZr)_5$.

The ductility was screened using first-principle DFT calculated shear G and bulk B moduli, by assessing inverse Pugh's ratio G/B empirical rule for a ductile material (Fig. 1d), i.e., $G/B < 0.57$–0.60[54,55]. The four compositions from Tier-1 screening all have inverse Pugh's ratios $G/B < 0.42$.

Tier-2 screening used more exhaustive calculations to examine the 4 alloys down-selected from the Tier-1 screening and also the neighboring space (±10 at.%) around each group (MoW), Ta, and (Ti,Zr). Four groups, each containing 8 compositions, were designed around the 4 alloys (Table 1 and Supplementary Table 1). Some compositions also included Al and Cr additions for enhanced oxidation resistance and density reduction considerations. The calculated properties for these 32 compositions include formation enthalpy (E_f), universal strength metric (r_s), shear modulus (G), bulk modulus (B), inverse Pugh's ratio (G/B), Poisson's ratio (v), and Young's modulus (E), as well as yield strength (σ_y) and its temperature dependence, through a model[56]. In Table 1, we have provided the universal metric r_s (for maximum strength[42]) and Young's moduli for the produced alloys. Given high B (~264 GPa) and E (~274 GPa) along with optimal formation energy (~−65 meV per atom) and Pugh's ratio (~0.42 < 0.57) range, the tier-2 down-selection process predicts AL-A6 and AL-A8 as best MPEAs. The AL-D6 and AL-D8 are two other MPEAs that fall in a similar category (based on B and E) as AL-A6 and AL-A8. However, they do not satisfy the optimal r_s and ductility criteria.

The DFT-based E_f suggests 32 compositions are all energetically stable in bcc (A2) phase (Fig. 2). It shows that adding Al enhances (Cr decreases) the MPEA stability. Singh et al.[29,53,57]. attributed the effect of Al addition on stabilizing the bcc phase to stronger electronic hybridization.

The valence-electron concentration (VEC) of the 32 compositions varies between 5.6 and 5.8, consistent with the formation of an A2 phase[29,58]. Though a VEC < 4.5 was suggested by Sheikh et al.[59] for intrinsic ductility for refractory high-entropy alloys, concentrated refractory alloys seem to deviate from this criterion[60]. Electronegativity difference on the Allen scale[61] was calculated to be 2–3%, which is not significant enough to favor the formation of intermetallics. Nearly all criteria for solid-solution formation are satisfied for the four groups of compositions. Notably, the failure mode or ductile–brittle transition in crystalline alloys is often connected to inverse Pugh's (G/B) and Poisson's (v) ratio[62] as G and B directly represent resistance to plastic deformation and fracture in polycrystalline materials, respectively. The inverse Pugh's ratio of these compositions is $0.35 \leq G/B \leq 0.43$, below the ductility criteria of <0.57[63] (see Supplementary Fig. 1), which allows initial filtering of useful RMPEAs.

Although tensile strength is most relevant (more on that below), e.g., for machinability, compressive strength for expediency is often reported in initial work. Hence, compressive yield-strength
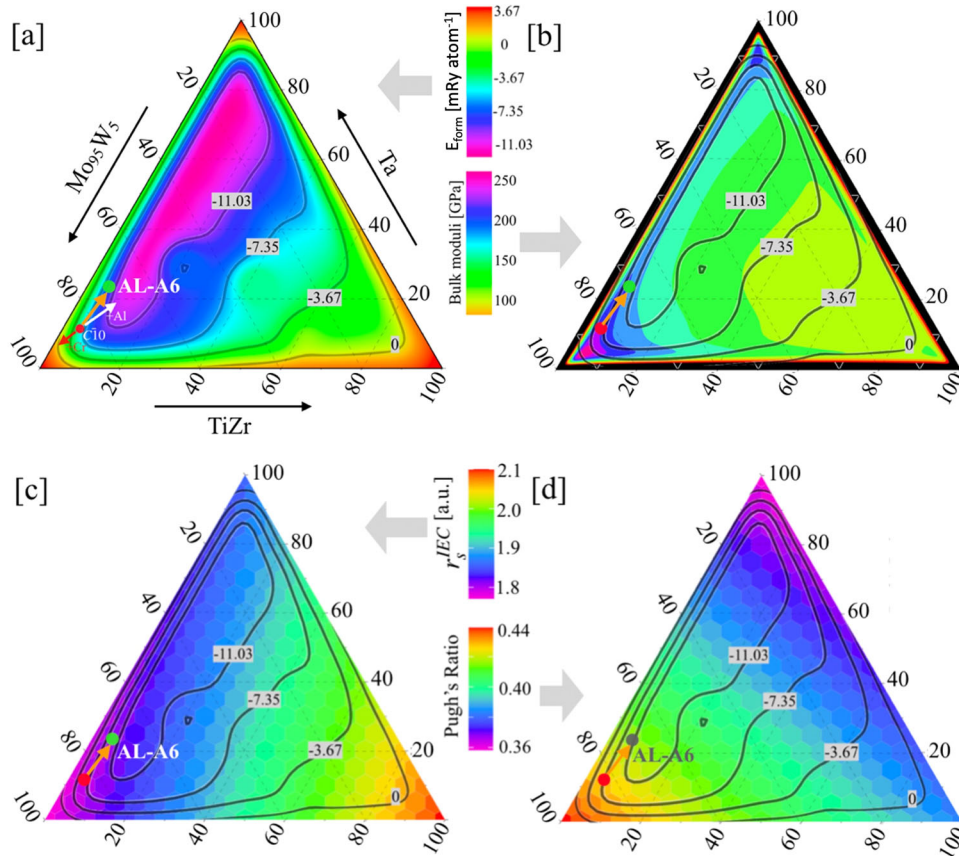
Fig. 1 Contour plots for (MoW)–Ta–(TiZr) system (Ti:Zr is fixed at 1). DFT E_f [meV] (**a**), hydrostatic, bulk compressive single crystal modulus B [GPa] (**b**), DFT universal strength metric r_s (**c**), and Pugh's ratio (G/B) (**d**); DFT results are derived from 0 K calculations.

Table 1. The nominal composition of 32 Ames Lab combinatorial arc-melted samples (AL) A1–A8, B1–B8, C1–C8, and D1–D8, along with DFT universal strength metric r_s and Young's moduli E.

ID	Nominal composition (at.%)							r_s	E	ID	Nominal composition (at.%)							r_s	E
	Mo	W	Ta	Ti	Zr	Al	Cr				Mo	W	Ta	Ti	Zr	Al	Cr		
ALA1	85	0	10	2.5	2.5	0	0	1.822	257.6	ALC1	80	0	10	5	5	0	0	1.837	237.1
ALA2	83.3	1.7	10	2.5	2.5	0	0	1.821	260.0	ALC2	78.4	1.6	10	5	5	0	0	1.836	246.3
ALA3	80.8	4.3	10	2.5	2.5	0	0	1.819	256.3	ALC3	76	4	10	5	5	0	0	1.835	249.7
ALA4	78.2	6.8	10	2.5	2.5	0	0	1.818	264.7	ALC4	73.6	6.4	10	5	5	0	0	1.833	247.3
ALA5	76.5	8.5	10	2.5	2.5	0	0	1.817	268.9	ALC5	72	8	10	5	5	0	0	1.832	240.1
ALA6	72.3	12.8	10	2.5	2.5	0	0	1.814	273.7	ALC6	68	12	10	5	5	0	0	1.83	241.0
ALA7	80.8	4.3	5	2.5	2.5	5	0	1.83	261.2	ALC7	76	4	5	5	5	5	0	1.846	240.4
ALA8	80.8	4.3	5	2.5	2.5	0	5	1.813	272.2	ALC8	76	4	5	5	5	0	5	1.828	243.6
ALB1	80	0	12.5	3.8	3.8	0	0	1.831	243.9	ALD1	80	0	20	0	0	0	0	1.812	260.1
ALB2	78.4	1.6	12.5	3.8	3.8	0	0	1.83	237.6	ALD2	78.4	1.6	20	0	0	0	0	1.811	266.1
ALB3	76	4	12.5	3.8	3.8	0	0	1.828	240.0	ALD3	76	4	20	0	0	0	0	1.81	267.1
ALB4	73.6	6.4	12.5	3.8	3.8	0	0	1.827	250.3	ALD4	73.6	6.4	20	0	0	0	0	1.808	270.8
ALB5	72	8	12.5	3.8	3.8	0	0	1.826	238.4	ALD5	72	8	20	0	0	0	0	1.807	255.8
ALB6	68	12	12.5	3.8	3.8	0	0	1.824	265.8	ALD6	68	12	20	0	0	0	0	1.805	270.4
ALB7	76	4	7.5	3.8	3.8	5	0	1.84	241.1	ALD7	76	4	15	0	0	5	0	1.821	265.3
ALB8	76	4	7.5	3.8	3.8	0	5	1.822	257.4	ALD8	76	4	15	0	0	0	5	1.803	272.8

(solid solution portion only throughout the paper) for these 32 compositions was evaluated using a yield-strength (σ_y) model described in the "Methods" section[29]. The model was validated 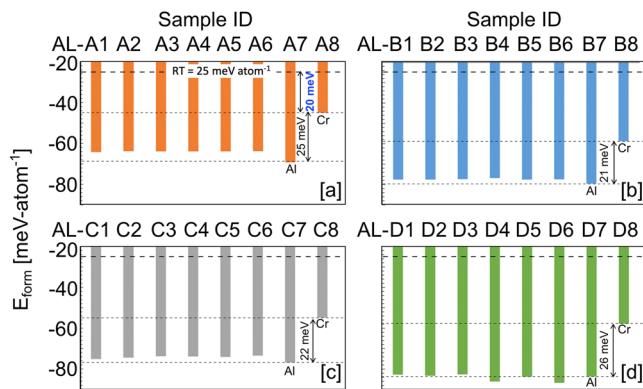using well-characterized MoNbTaW and MoNbTaVW alloys[25]. At RT, the DFT-calculated and experimentally measured values are (σ_y^{DFT}, σ_y^{EXP}) = (970, 1058) MPa for MoNbTaW and (1170, 1246) MPa for MoNbTaVW[25]. Similarly, at 1300 °C, (σ_y^{DFT}, σ_y^{EXP}) = (367, 450) MPa for MoNbTaW and (655, 700) MPa for MoNbTaVW[25].

To understand the temperature dependence of elastic properties, we fitted the DFT-calculated Young's modulus E (0 K) using a linear model proposed by Wachtman et al.[64] at 300 K, which was later applied to C_{ij}'s by Steneteg et al.[65]. These DFT results agree with our measurements at RT with an average error < 1% (Fig. 3a). The insignificant change of E modulus is reasonable as the changes in bonding and thermal expansion from 0 K to RT are small (as expected from Grüneisen theory)[66–68]. Extrapolating from RT to 1300 °C, E drops more noticeably, by an average of 7.5% (Fig. 3b). Those compositions with higher melting temperature drop less, whereas the ones with lower melting temperature, e.g., Al-doped samples, show the largest drop (15%). This suggests that maximizing the melting temperature for MPEAs may maximize mechanical properties (a strategy however that has an adverse impact on RT ductility), which is well explained by the modulus-temperature relationship $E(T)/E(0) = [1 - \alpha(T/T_m)]$, where E is the modulus at temperature T in Kelvin ($E(0)$ is at 0 K) and α is a constant of order 0.5[69].

Rapid sample preparation and verification

These 32 compositions were synthesized and characterized using a set of HTP methods tailored for this study. Small samples (1.5 g each) were prepared using a combinatorial arc melting system capable of making 32 samples in one run. The obtained samples were characterized for compositions using scanning X-ray fluorescence (XRF), crystal structures and phases using X-ray diffraction, density using the Archimedes' method, elastic moduli (E, G, ν) using ultrasonic pulse-echo measurement, and σ_y using RT compression test.

The as-cast samples (quench rate ~10^3 °C/s) are all nearly a single solid solution A2 (bcc) phase based on X-ray diffraction analysis (Fig. 4a–d). The measured lattice parameters match well with DFT optimized results (Fig. 4e) for group AL-A and AL-D,
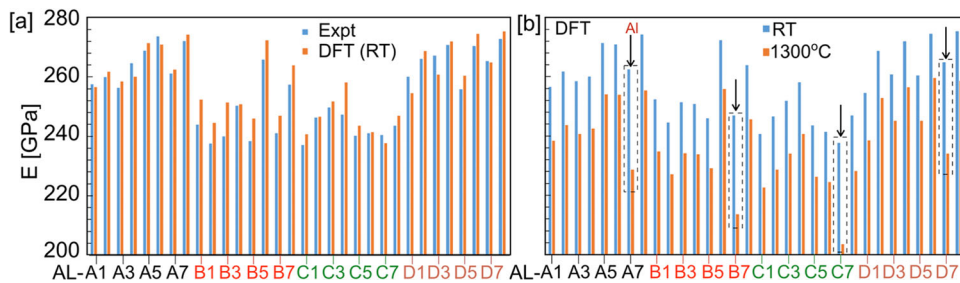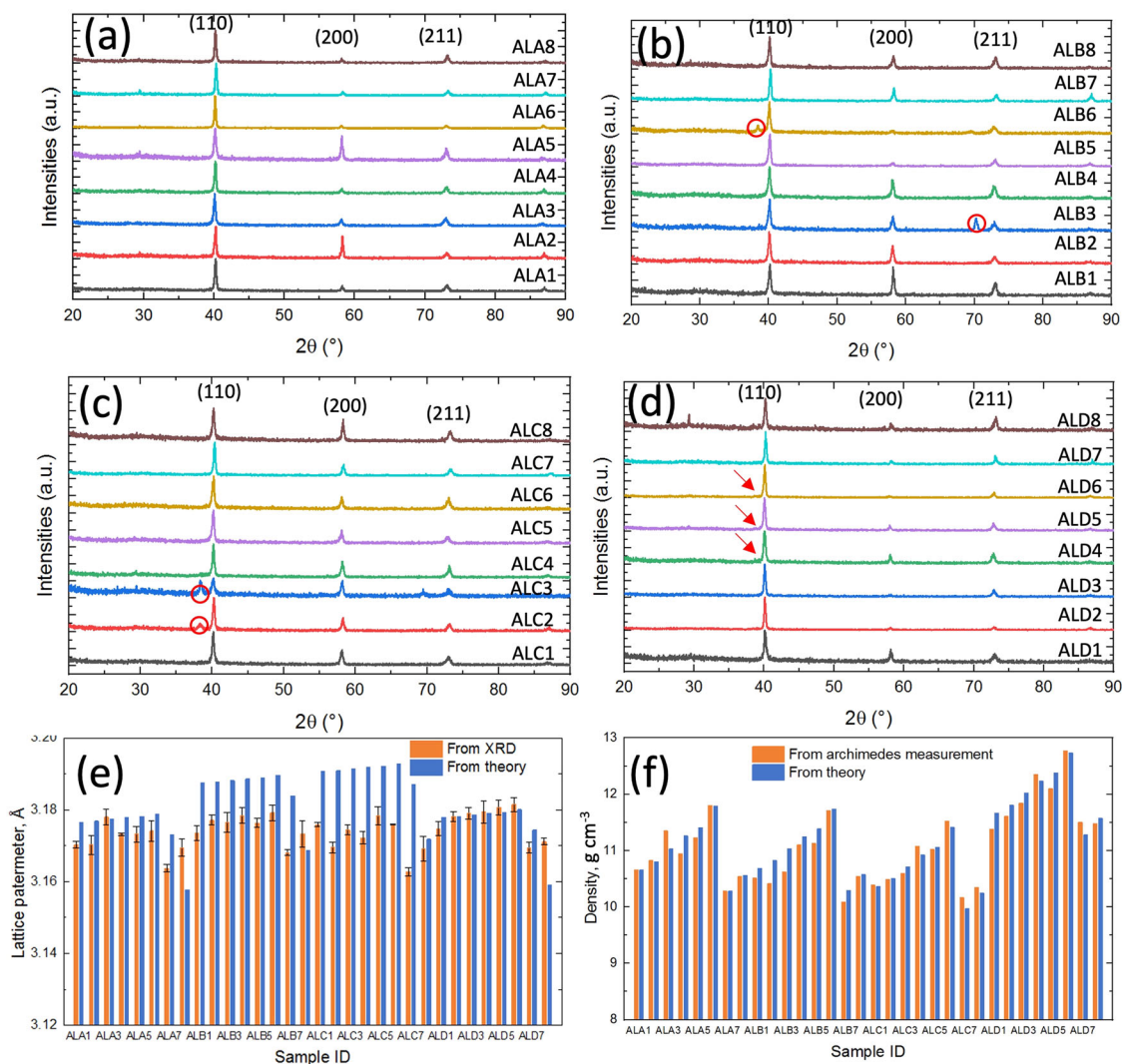
while only a very small deviation was observed for group AL-B and AL-C, indicating that the as-cast samples form a continuous solid solution across the phase space[29]. The densities of all samples are over 10 g/cm³ (Fig. 4f). The experimentally measured densities agree well with a rule-of-mixture estimate from the individual elements, again indicating solid-solution formation rather than intermetallic compound formation. Though the densities of RMPEAs are higher than typical nickel superalloys, their specific strengths are higher, especially above 1000 °C as shown below.

Standard size sample preparation and characterization

Based on the measured density, melting point, strength metric, and RT moduli, samples AL-A3: $(Mo_{95}W_5)_{85}Ta_{10}(TiZr)_5$, AL-A6: $(Mo_{85}W_{15})_{85}Ta_{10}(TiZr)_5$, and AL-A8: $(Mo_{95}W_5)_{85}Ta_5(TiZr)_5Cr_5$ were selected for a detailed Tier 3 screening, showing good a priori strength metric. The AL-A3 alloy was selected for its relatively low density while having a high melting point and modulus; AL-A6 was selected for its high melting point and high modulus; AL-A8 was selected for its low density, strength metric, and high modulus.

The as-cast AL-A3, A6, and A8 exhibit dendritic structures typical for arc-melted RMPEA due to constitutional segregation during solidification[8,9,29]. The samples remain solid solution going from tier 2 (1.5 g) to tier 3 selection (~50 g) though there were minor reductions in the cooling rate with the larger mass. It is not clear if the identified alloys will remain solid solutions after casting when the size of the cast material is scaled up to kg or higher. Scaling may be addressed by powder metallurgy approaches like gas atomization followed by hot-isostatic-press approach. The Z contrast in the backscattered SEM images (Fig. 5) shows that the dendrites are enriched while the interdendritic regions are depleted in higher T_m atoms. The EDS line scan across the dendrites further confirms that the heavier atoms W and Ta are concentrated in the dendritic region while the lighter elements Zr, Ti, and Cr are concentrated in the interdendritic region.

Mechanical properties by compression test. The yield strength $\sigma_{0.2}$ and compressive strain before fracture for AL-A3, A6, and A8 are (820 MPa, 10.0%), (760 MPa, 9.2%), and (750 MPa, 7.8%), respectively (Fig. 6). An equiatomic MoNbTaW that has high strength but limited ductility, based on the work by Senkov et al.[25] was prepared and tested in the same manner. The results show that MoNbTaW has higher $\sigma_{0.2}$ (1010 MPa) but less compressive strains (2.8%) than A3, A6, and A8. AL-A6 was also tested at 1300 °C in compression. The compressive yield strength at 1300 °C for Al-A6 is 446 MPa, similar to MoNbTaW (460 MPa) and less than MoNbTaVW (655 MPa)[25]. However, AL-A6 is 3× more ductile than the equiatomic MPEAs and shows less temperature dependence of its yield strength. The high W content in MoNbTaW alloy likely contributed to its high yield strength, increased density, and reduced ductility. AL-A3, A6, and A8 have larger atomic size differences ($\delta = 2.64$, 2.62, and 3.22, respectively) than MoNbTaW ($\delta = 2.28$), which may boost yield strength due to increased solute-induced stress[26], but not enough to be


Fig. 2 DFT formation energy E_f of the 32 samples. Ames Lab (AL) A1–A8 (**a**), B1–B8 (**b**), C1–C8 (**c**), and D1–D8 (**d**). RT equivalent energy is denoted (horizontal dashed line) at 25 meV atom⁻¹. Aluminum additions enhance MPEAs stability (E_f is more negative), while Cr decreases stability (E_f is less negative).

Fig. 3 Young's moduli, E, by experimental and DFT. Comparison between RT experimental and DFT Young's moduli, E (**a**), showing good agreement; E at 1300 °C shows a minor drop from RT values; however, E decays much faster (as marked) on Al added samples MPEAs (**b**).

Fig. 4 Phase information, lattice parameter, and density of the 32 samples. XRD pattern of the samples (**a–d**). Lattice parameter from theory and from XRD (**e**). Density from the rule of mixtures and Archimedes measurement (**f**). Compositions of the 32 samples can be found in Table 1 and Supplementary Table 1.

comparable to MoNbTaW. AL-A8 has the highest δ due to the introduction of smaller and lighter Cr atoms, and it has the highest specific yield strength. The improved ductility can be partly attributed to the Ti and Zr added to the alloys, which includes filling a favorable electronic dispersion at the Fermi energy[29], enhancing the atomic interstitial electron density of the metal and thus its strength[42]. Similar effects of Ti and Zr on improving ductility were observed for HfNbTaTiZr[26], AlHfNbTaTiZr[70], HfMoNbTiZr[71], HfNbTiVZr[72], and NbTiVZr[73] alloys. Compared to systems reported by Tseng et al.[28] (HfMoNbTaTi, HfMoNdTaZr, and HfMoTaTiZr), the yield strength of AL-A6 is much higher than that of HfMoTaTiZr and comparable to the other two at 1300 °C. AL-A6 also shows higher ductility than HfMoTaTiZr, although it is not as ductile at RT as the other two (see Table 2). Tseng et al.[28] contribute higher ductility to the Nb addition. As Nb has the same VEC as Ta, we did not include Nb in our current HTP study. It should be noted that since Nb and Ta can have large differences when interacting with Ti and Zr, the phase formation and ductility can differ significantly.

Tensile and creep properties by small punch test. While most literature only reports compressive properties, tensile properties are of the most engineering importance. It was shown that small punch tests (SPT) provide tensile yield strength when the small-

size membrane sample is punched through undergoing a stretching deformation[74]. Our SPT results show that the yield points for as-cast AL-A3, A6, and A8 are 150, 240, and 193 MPa at 1300 °C, respectively (Fig. 7). The SPT strength of ALA6 is considerably higher than that of TZM (Mo–0.5%Ti–0.1%Zr alloy, ASTM B386 TYPE 364) (~110 MPa) and H282 (~20 MPa) at 1300 °C. We also carried out SPT on equiatomic MoNbTaW and MoNbTaVW, they all fractured before any meaningful loading. The deformed regions of the as-cast samples in Fig. 7a assume half-dome shapes, indicating a significant degree of ductility. The fractured surfaces of the samples punch tested at 1300 °C (Fig. 7c–e) offer additional insights into the fracture behavior. The as-cast samples show river patterns, cleavage feathers, and shear ledges on the fractured surface, indicating a quasi-ductile transgranular fracture mechanism.

AL-A3, A6, and A8 alloys are all highly creep resistant, with AL-A6 exceeding the properties of any known refractory alloys. Small punch creep (SPC) tests were conducted at 1000 and 1300 °C with 200 and 100 MPa for up to 100 h, respectively. The SPC creep deformation curves are shown in Fig. 8 for AL-A6, a typical fully age-hardened Ni-based superalloy Haynes 282, and a typical refractory alloy TZM, consolidated via powder metallurgy route. All the samples entered the steady-state creep stage without rupture at the
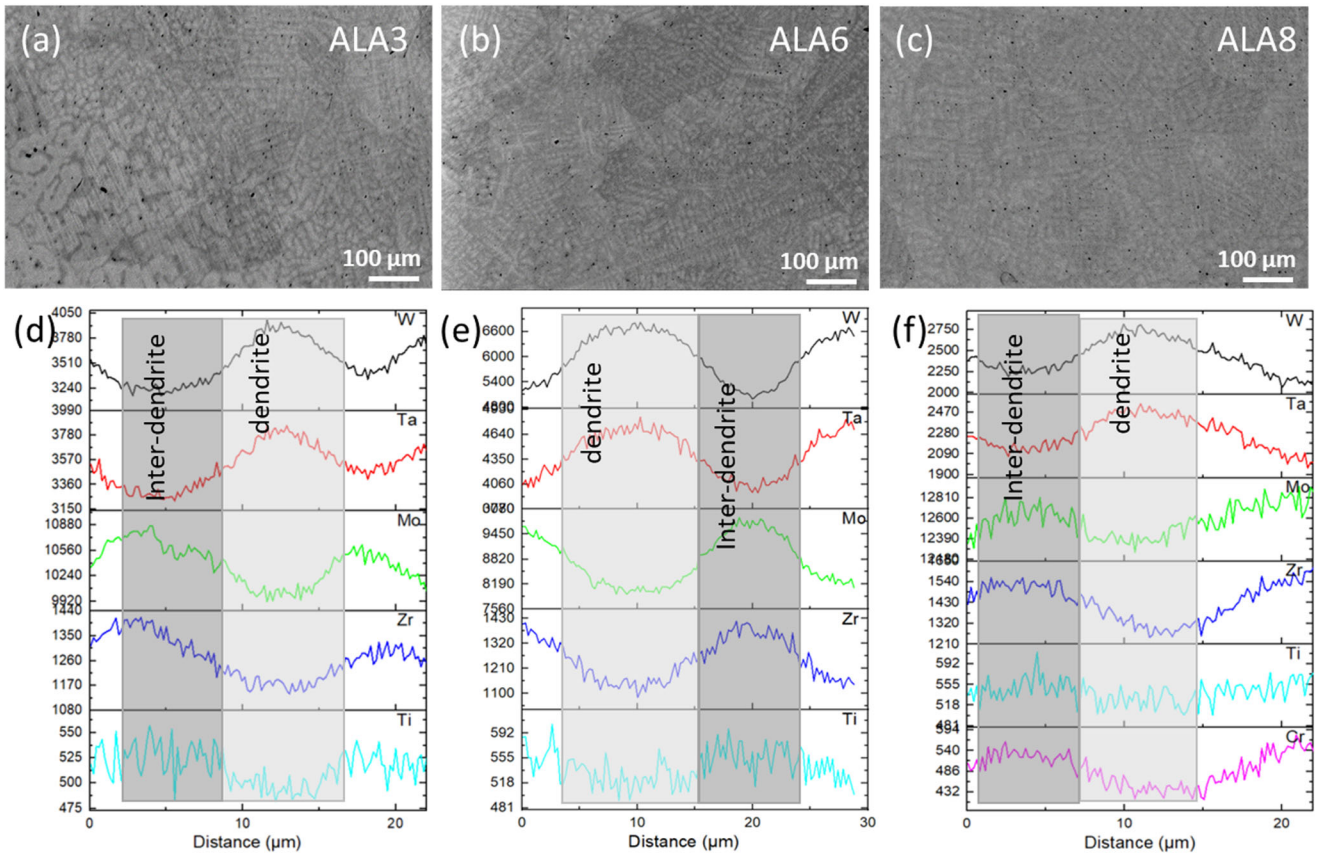
Fig. 5 Microstructure and compositional information of the as-cast samples. SEM backscattered images of ALA3 (**a**), ALA6 (**b**), and ALA8 (**c**) samples. EDS line scan showing the element distribution for ALA3 (**d**), ALA6 (**e**), and ALA8 (**f**) samples.

100th hour. At 1000 °C 200 MPa, the minimum creep rate of AL-A6 is $1.55 \times 10^{-5} \, h^{-1}$, much lower than that of Haynes-282 ($2.56 \times 10^{-4} \, h^{-1}$) and TZM ($2.83 \times 10^{-4}$) tested under the same condition. Haynes-282 was not tested at 1300 °C due to its low melting point 1348 °C. AL-A6 maintained a low creep rate $2.99 \times 10^{-5} \, h^{-1}$ even at 1300 °C 100 MPa. The creep resistance of AL-A6 is partially a result of its high melting points, as it is creep tested at 42–53% melting point where solid-solution strengthening still dominates. The large lattice strain and atomic-size mismatch from the multiple elements may also contribute to the increase in resistance to dislocation initiation and multiplication.

AL-A6 exhibits a good combination of RT ductility and HT strength, but its oxidization resistance is poor, which is typical for Mo-based alloys. To address this concern when deploying the alloy for application, we developed a multilayer RMPEA-Si-B coating (including a Mo precoating and a Si–B pack cementation)[75,76]. The coating is chemically compatible with AL-A6 and provides significant improvement in oxidation resistance compared to the uncoated sample. At both isothermal and cyclic conditions at 1300 °C, the mass changes for the coated samples are $2.7 \, mg \, cm^{-2}$ after 50 h in thermal condition and $1 \, mg \, cm^{-2}$ after 400 cycles in cyclic condition. The improved oxidation resistance by the coating is provided by its multilayered structure, where the top aluminoborosilicate acts as an oxygen barrier, a disilicide layer as source for silica formation, a boron-doped $(metal)_5Si_3$ T1 layer for oxidation resistance, and a $(metal)_5Si_2B_2$ T2 and boride layer acts as a diffusion barrier and provides boron for T1 layer generation and for long term stability (see details in refs. [75,77]).

In summary, we showcased accelerated (~1 year) discovery of RMPEAs with an improved combination of RT and HT mechanical properties by combining DFT-guided down-selection with rapid alloy synthesis and characterization. For rapid screening, we used

four simple criteria, including the use of a universal metric for a priori down-selection of alloy compositions with higher strength, and identified $Mo_{72.3}W_{12.8}Ta_{10.0}Ti_{2.5}Zr_{2.5}$ with well-balanced compressive, tensile, and creep properties up to 1300 °C. In combination with a borosilicate (self-healing) coating, this alloy is also resistant to oxidation at 1300 °C.

METHODS

Calculation of mechanical properties

The reduced model for the zero-temperature shear yield-stress developed by Maresca and Curtin[78] is represented by an analytical equation governed by the stiffness constants (C_{ij}'s):

$$\tau_{y0} = 0.04 \alpha^{-\frac{1}{3}} \bar{\mu} \left(\frac{1+\bar{\nu}}{1-\bar{\nu}} \right)^{\frac{4}{3}} \left[\frac{\sum_n c_n \Delta V_n^2}{\bar{b}^6} \right] \quad (1)$$

where α is the edge dislocation line tension parameter, $\bar{\mu}$ is the shear moduli, $\bar{\nu}$ is Poisson's ratio, c_n is the concentration of type n solute, ΔV_n is the misfit volume of type n solute, and $\bar{b}$ is the Burger's vector. The $\bar{\mu}$, $\bar{\nu}$, and $\bar{B}$ (bulk moduli) are related to C_{ij}'s by

$$\bar{\mu} = \sqrt{\frac{1}{2} C_{44}(C_{11} - C_{12})} \quad (2)$$

$$\bar{B} = (C_{11} + 2C_{12}) \quad (3)$$

$$\bar{\nu} = \frac{3\bar{B} - 2\bar{\mu}}{2(3\bar{B} + \bar{\mu})} \quad (4)$$

The DFT-calculated stiffness constants, elemental elastic parameters and alloy volumes were used to estimate the C_{ij}'s. The misfit volume
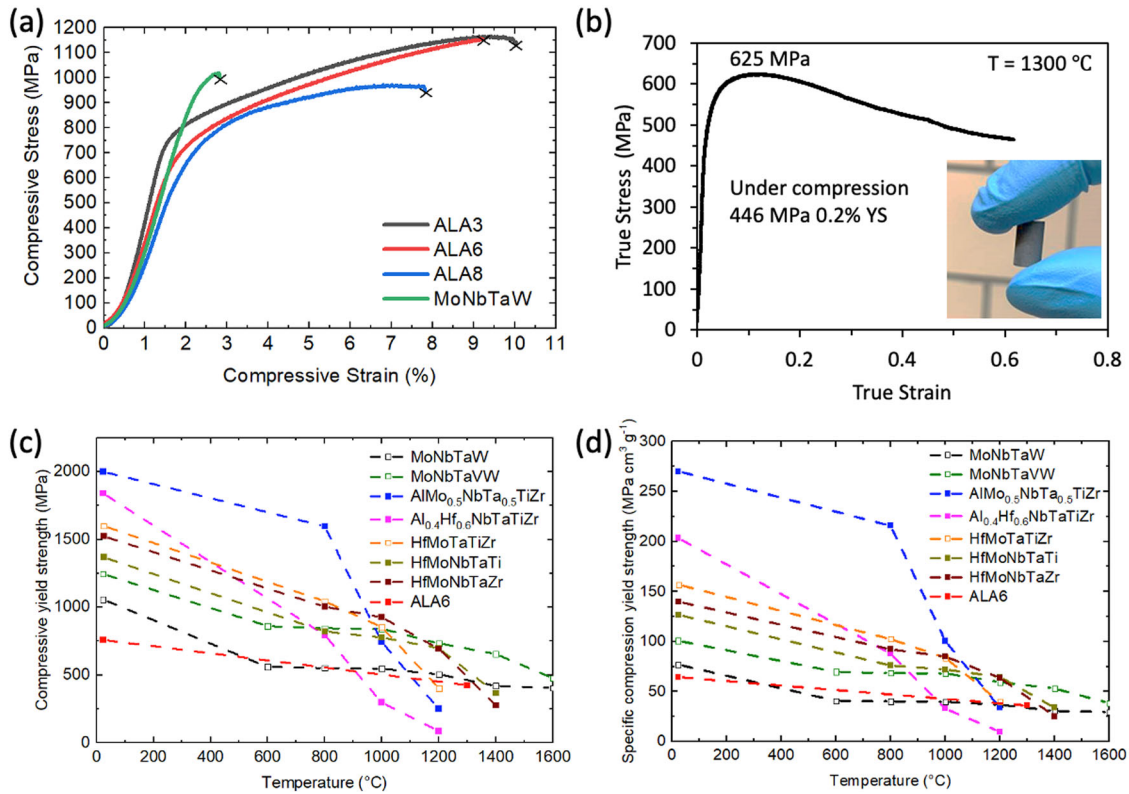
Fig. 6 Compressive properties of the samples. Compression stress–strain curves at RT for AL-A3, A6, A8 samples (**a**); at 1300 °C for ALA6 (**b**); and comparison of compressive yield strength (YS) (**c**) and specific compressive YS (**d**) of ALA6 with other MPEAs[11,14,36]—open (filled) symbols show <5% RT (≥10% RT) fracture strain.

Table 2. Density and compressive (RT and 1300 °C) properties for AL-A3, A6, A8, Mo NbTaW, HfMoNbTaTi, HfMoNbTaZr, and HfMoTaTiZr.

Sample	Room temperature				1300 °C	
	Density (g cm^{-3})	0.2% YS (MPa)	Specific 0.2% YS (MPa cm^3 g^{-1})	Total strain (%)	0.2% YS (MPa)	Specific 0.2% YS (MPa cm^3 g^{-1})
AL-A3	11.4	820	71.9	10.0		
AL-A6	11.8	760	64.4	9.2	446	37.8
AL-A8	10.5	750	71.4	7.8		
MoNbTaW	13.7	1010	73.9	2.8	460	33.6
HfMoNbTaTi	10.8	1369	126.8	27	530	49.1
HfMoNbTaZr	10.9	1524	139.8	16	485	44.5
HfMoTaTiZr	10.2	1600	156.9	4	175	17.2

The 1300 °C data for MoNbTaW, HfMoNbTaTi. HfMoNbTaZr, and HfMoTaTiZr are extrapolated from the references[28] via linear interpolation. Densities of HfMoNbTaTi. HfMoNbTaZr, and HfMoTaTiZr are calculated via weighted averages. Note that the specific strength of Haynes-282 at 1300 °C is ≤3 MPa cm^3 g^{-1}.

was estimated from the rule of mixture. The model was fitted with the rule-of-mixtures stiffness constants, and this fitting parameter is absorbed by the 0.04 value making it just a scaling factor.

At finite temperature and finite strain rate standard thermal activation theory then leads to the predicted tensile yield stress as: (with k Boltzmann's constant, T (in Kelvin)

$$\sigma_{y0} = 3.0\tau_{y0}\left[1 - \left(\frac{kT}{\Delta E_b}\ln\frac{\dot{\epsilon}_0}{\dot{\epsilon}}\right)^{2/3}\right] \quad (5)$$

Here, 3.06 is the Taylor factor for isotropic bcc polycrystal strength controlled by edge dislocations, $\dot{\epsilon}_0$ is a reference strain rate. The quantities $\bar{\mu}$ and $\bar{v}$ are the shear modulus and Poisson's ratio of the alloy, and 0.0833 (bcc) is related to the edge dislocation line tension as $\Gamma = \alpha\bar{\mu}b^2$. The experimental Poisson's ratio was used in strength calculation.

Combinatorial synthesis and characterization

A set of 32 samples (1.5 g each) were synthesized with a generalized formula of $(Mo1-aWa)\times Tay(TiZr)zAl\beta Cr\gamma$ using the combinatorial arc-melt system (SP-MAM32, MTI Corporation). High-purity elemental raw materials (at least 99.9% pure) were acquired from the Materials Preparation Center at Ames Laboratory. The starting materials were in the form of foil or wire for convenient handling. Synthesized samples were machined into a cylinder shape ~3 mm in height with parallel top and bottom surfaces using an electrical discharge machining (EDM). Elastic moduli were measured using the ultrasound pulse-echo technique. Modulus was calculated by from:

$$\text{Poisson's ratio } v = \frac{1 - 2(V_T/V_T)^2}{2 - 2(V_T/V_T)^2} \quad (6)$$

$$\text{Young's modulus } E = \frac{V_L^2\rho(1+v)(1-2v)}{1-v} \quad (7)$$

where V_T is the shear (transverse) velocity, V_L is the longitudinal velocity, ρ is the density, and v is the Poisson's ratio of the samples. The densities of the samples were measured by Archimedes' method[79]. To compute for shear and longitudinal velocities (V_T and V_L), the respective round-trip transit time values were measured by a precision thickness gauge (38DL PLUS, Olympus) with shear wave (V156, Olympus) and longitudinal wave (M112, Olympus) contact transducer. The velocity was calculated by dividing sample thickness by one-half of the round-trip transit time. The compositions of samples were
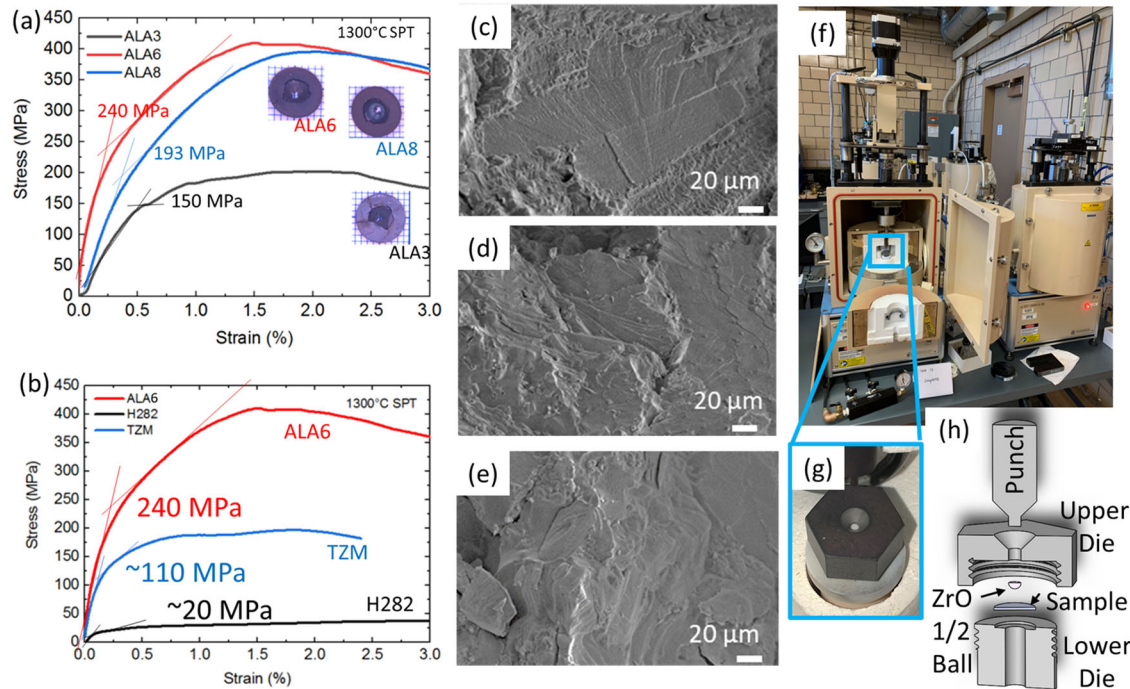
Fig. 7 Small punch test results at 1300 °C and its setup. Stress versus strain curves for AL-A3, A6, and A8 (**a**), and for AL-A6, TZM (Mo–0.5% Ti–0.1%Zr alloy), and Haynes-282 (**b**). SEM images of fracture surfaces after 1300 °C punch tests for ALA3 (**c**), ALA6 (**d**), and ALA8 (**e**); small-punch rig setup (**f**), die (**g**), and schematics (**h**). Samples were tested in an inert atmosphere and not coated.
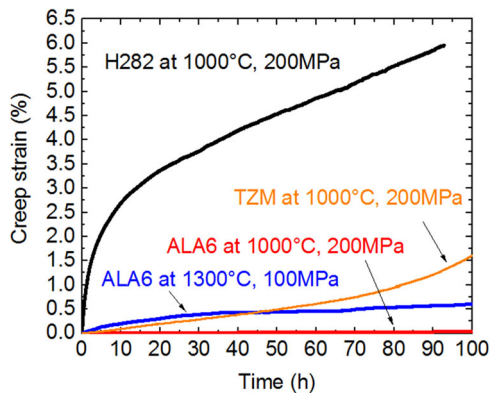
Fig. 8 Small punch creep tests of H282, TZM, and AL-A6 samples at 1000 and 1300 °C. Load is 7.88 kg (200 MPa) for 1000 °C and 3.94 kg (100 MPa) for 1300 °C. Thickness for the samples ranges from 0.42 to 0.43 mm. The minimum creep rates are 2.54×10^{-4}, 2.83×10^{-4}, 1.54×10^{-5}, 3.00×10^{-5} h^{-1} for H282 at 1000 °C, TZM at 1000 °C, AL-A6 at 1000 °C, and AL-A6 at 1300 °C, respectively. The inflection at ~70 h for TZM reflects a partial crack in the sample.

measured by energy-dispersive spectroscopy (EDS) on a scanning electron microscope (SEM) (Teneo, FEI Inc). X-ray diffraction patterns were acquired using a Bruker DaVinci D8 diffractometer with a Cu target equipped with an autosampler.

Standard-size sample preparation, testing, and characterization

Down-selected standard-sized samples (10–20 g) were synthesized by arc melting of elemental pure metal sheets (at least 99.9% pure) acquired from the Materials Preparation Center at Ames Laboratory. Samples were flipped five times during the process to ensure homogeneity. Cylinders (2 mm in diameter and 6mm in length) and disks (8 mm in diameter and 0.5 mm in thickness)

were EDM machined from arc-melted buttons for RT compression tests and HT small punch tests, respectively. The RT compression tests were conducted on an Instron 5569 testing frame with a 0.2 mm min^{-1} loading rate following a modified ASTM E9-19 standard[80] due to the small sample size. The small punch tests were conducted on a compact small punch rig (OTF-1500X-S-ST, MTI Corporation) co-designed by the authors and MTI corporation following European standards on small-punch testing of metallic materials[81] with 0.5 mm/min loading rate in flowing Ar atmosphere. The punch die set is made of SiC (OTF-1500X-S-CR-SIC, MTI Corp.), the punch rod is made of Mo (OTF-1500X-S-CR-MO, MTI Corp.), and the half-ball that transfers the force to the sample is made from ZrO_2 with a diameter of 2.5 mm. Yield point was determined from load–displacement curve via an empirical relationship:

$$S_y = \alpha \frac{P_y}{t^2} \tag{8}$$

where S_y is the tensile yield, P_y is the load at yield, t is the sample thickness, and α is a geometry-dependent correlation coefficient (0.479 in our case)[74,81]. For the small punch creep tests (SPC), the same mold and sample geometry was used, the load was applied by a dead load system when the target temperature has reached, and the creep stress was evaluated using Eq. (8). The SPC tests were conducted in a flowing Ar atmosphere for up to 100 h. The minimum creep rate was calculated using an empirical equation:

$$\dot{\varepsilon}_{min} = 0.3922 \, \dot{v}_{min}^{1.191} \, [1/h] \tag{9}$$

where $\dot{\varepsilon}_{min}$ is the minimum creep rate, $\dot{v}_{min}$ is the minimum creep deformation rate as determined from plotting the second derivative of the creep deformation curve.

The strain in the SPT and SPC plots were calculated assuming the stain accumulates in the radial direction of the sample via the following equation:

$$\varepsilon = \frac{\Delta l}{l_0 + \Delta l} = \frac{\text{sqrt}(0.5D^2 + v^2) - 0.5D}{0.5D + \text{sqrt}(0.5D^2 + v^2) - 0.5D} \times 100\% \tag{10}$$

where ε, Δl, and l_0 are the strain, change in gauge length, and initial gauge length, respectively. D is the diameter of the lower punch opening, and v is the displacement from the LVDT.

The HT compression test was conducted in a vacuum of 10^{-5} Torr or better with an initial strain rate of $10^{-3}\,s^{-1}$ using an Instron mechanical testing machine fitted with a vacuum furnace. Cylindrical specimens with a diameter of ~6.5 mm and a height of ~11mm were used for the test. The cross-sectional and fractured-surface imaging was done using a scanning electron microscope (SEM) (Teneo, FEI Inc.) equipped with an energy-dispersive X-ray spectroscopy (EDS) detector.

Density-functional theory (DFT)

The all-electron, DFT-based Korringa–Kohn–Rostoker (KKR) Greens' function method combined with the coherent potential approximation (CPA) was used to calculate total energy, lattice parameters, universal strength metric, and moduli of arbitrary solid-solution alloys[47]. The KKR-CPA performs averaging overall all possible configurations simultaneously with DFT charge self-consistency, which properly includes alloy-induced Friedel impurity-charge screening and core-level shifts due to alloying. As such only small symmetry-equivalent unit cells are required, e.g., 1-atom (2-atom) cells for A1/A2 (A3). Hence, thousands of alloy compositions can be performed in an HTP manner. For defected cells (e.g., stacking faults) larger unit cells are required but the configurational averages are fully performed over the full cell. We used the Perdew–Burke–Ernzerhof (PBE) exchange-correlation functional for solids[82]. We employed a site-centered, spherical-harmonic basis with s, p, d, and f-orbital symmetries (i.e., $L_{max} = 3$) in all calculations. The self-consistent charge density was obtained from Green's function using a complex-energy contour integration and Gauss-Laguerre quadrature (with 24 energy points on a semi-circular mesh enclosing the bottom to the top of the valence states). An equally spaced Monkhorst–Pack k-space mesh of $24 \times 24 \times 24$ for bcc/fcc was used for Brillouin zone integrations. Core electrons were treated fully relativistically (which includes spin–orbit coupling), while semi-core/valence electrons were treated scalar relativistically (neglecting spin–orbit coupling).

DATA AVAILABILITY

The authors declare that the data supporting the findings of this study are available within the paper and supplement. Also, the data that support the plots within this paper and other findings of this study are available from the corresponding author upon reasonable request.

REFERENCES

1. McQueen, S. et al. *Department of Energy Hydrogen Program Plan*. https://www.hydrogen.energy.gov/pdfs/hydrogen-program-plan-2020.pdf (2020)
2. Perepezko, J. H. The hotter the engine, the better. *Science* **326**, 1068–1069 (2009).
3. Glassman, I. *Combustion* 2nd edn (Elsevier, 2012).
4. Caron, P. High γ' solvus new generation nickel-based superalloys for single crystal turbine blade applications. *Superalloys* **2000**, 737–746 (2000).
5. Darolia, R. Development of strong, oxidation and corrosion resistant nickel-based superalloys: critical review of challenges, progress and prospects. *Int. Mater. Rev.* **64**, 355–380 (2019).
6. ULTIMATE | Ultrahigh Temperature Impervious Materials Advancing Turbine Efficiency. https://arpa-e.energy.gov/technologies/programs/ultimate (2020).
7. Senkov, O. N., Miracle, D. B., Chaput, K. J. & Couzinie, J.-P. Development and exploration of refractory high entropy alloys—a review. *J. Mater. Res.* **33**, 3092–3128 (2018).
8. Miracle, D. B. & Senkov, O. N. A critical review of high entropy alloys and related concepts. *Acta Mater.* **122**, 448–511 (2017).
9. Senkov, O. N., Wilks, G. B., Miracle, D. B., Chuang, C. P. & Liaw, P. K. Refractory high-entropy alloys. *Intermetallics* **18**, 1758–1765 (2010).
10. Yeh, J.-W. et al. Nanostructured high-entropy alloys with multiple principal elements: novel alloy design concepts and outcomes. *Adv. Eng. Mater.* **6**, 299–303 (2004).
11. Lai, W. et al. Design of BCC refractory multi-principal element alloys with superior mechanical properties. *Mater. Res. Lett.* **10**, 133–140 (2022).
12. Yang, T. et al. Multicomponent intermetallic nanoparticles and superb mechanical behaviors of complex alloys. *Science* **362**, 933–937 (2018).
13. George, E. P., Raabe, D. & Ritchie, R. O. High-entropy alloys. *Nat. Rev. Mater.* **4**, 515–534 (2019).
14. Zhang, Y. et al. Microstructures and properties of high-entropy alloys. *Prog. Mater. Sci.* **61**, 1–93 (2014).
15. Seol, J. B. et al. Boron doped ultrastrong and ductile high-entropy alloys. *Acta Mater.* **151**, 366–376 (2018).
16. Moon, J. et al. Unraveling the discontinuous plastic flow of a Co–Cr–Fe–Ni–Mo multiprincipal-element alloy at deep cryogenic temperatures. *Phys. Rev. Mater.* **5**, 083601 (2021).
17. Gludovatz, B. et al. A fracture-resistant high-entropy alloy for cryogenic applications. *Science* **345**, 1153–1158 (2014).
18. Jo, Y. H. et al. Cryogenic strength improvement by utilizing room-temperature deformation twinning in a partially recrystallized VCrMnFeCoNi high-entropy alloy. *Nat. Commun.* **8**, 15719 (2017).
19. Shi, Y., Yang, B. & Liaw, P. K. Corrosion-resistant high-entropy alloys: a review. *Metals* **7**, 43 (2017).
20. Qiu, Y., Thomas, S., Gibson, M. A., Fraser, H. L. & Birbilis, N. Corrosion of high entropy alloys. *Npj Mater. Degrad.* **1**, 1–18 (2017).
21. Nene, S. S. et al. Corrosion-resistant high entropy alloy with high strength and ductility. *Scr. Mater.* **166**, 168–172 (2019).
22. Shi, Y. et al. Homogenization of AlxCoCrFeNi high-entropy alloys with improved corrosion resistance. *Corros. Sci.* **133**, 120–131 (2018).
23. Zhang, Z., Han, E.-H. & Xiang, C. Corrosion behaviors of Mo0.5NbTiVCr0.25 and Mo0.5NbTiV0.5Zr0.25 multi principal element alloys in high temperature borated and lithiated water. *Corros. Sci.* **206**, 110514 (2022).
24. Senkov, O. N., Miller, J. D., Miracle, D. B. & Woodward, C. Accelerated exploration of multi-principal element alloys with solid solution phases. *Nat. Commun.* **6**, 6529 (2015).
25. Senkov, O. N., Wilks, G. B., Scott, J. M. & Miracle, D. B. Mechanical properties of Nb25Mo25Ta25W25 and V20Nb20Mo20Ta20W20 refractory high entropy alloys. *Intermetallics* **19**, 698–706 (2011).
26. Senkov, O. N., Scott, J. M., Senkova, S. V., Miracle, D. B. & Woodward, C. F. Microstructure and room temperature properties of a high-entropy TaNbHfZrTi alloy. *J. Alloys Compd.* **509**, 6043–6048 (2011).
27. Senkov, O. N. et al. Microstructure and elevated temperature properties of a refractory TaNbHfZrTi alloy. *J. Mater. Sci.* **47**, 4062–4074 (2012).
28. Tseng, K.-K. et al. Effects of Mo, Nb, Ta, Ti, and Zr on mechanical properties of equiatomic Hf–Mo–Nb–Ta–Ti–Zr alloys. *Entropy* **21**, 15 (2019).
29. Singh, P. et al. Design of high-strength refractory complex solid-solution alloys. *Npj Comput. Mater.* **4**, 1–8 (2018).
30. Gorsse, S., Couzinié, J.-P., & Miracle, D. B. From high-entropy alloys to complex concentrated alloys. *C. R. Phys.* **19**, 721–736 (2018).
31. Springer, H. & Raabe, D. Rapid alloy prototyping: compositional and thermo-mechanical high throughput bulk combinatorial design of structural materials based on the example of 30Mn–1.2C–xAl triplex steels. *Acta Mater.* **60**, 4950–4959 (2012).
32. Zhao, J.-C., Zheng, X. & Cahill, D. G. High-throughput diffusion multiples. *Mater. Today* **8**, 28–37 (2005).
33. Lee, C. et al. An experimentally driven high-throughput approach to design refractory high-entropy alloys. *Mater. Des.* **223**, 111259 (2022).
34. Feng, R. et al. High-throughput design of high-performance lightweight high-entropy alloys. *Nat. Commun.* **12**, 4329 (2021).
35. Khakurel, H. et al. Machine learning assisted prediction of the Young's modulus of compositionally complex alloys. *Sci. Rep.* **11**, 17149 (2021).
36. Wen, C. et al. Machine learning assisted design of high entropy alloys with desired property. *Acta Mater.* **170**, 109–117 (2019).
37. Vela, B. et al. High-throughput exploration of the WMoVTaNbAl refractory multi-principal-element alloys under multiple-property constraints. *Acta Mater.* **248**, 118784 (2023).
38. Sorkin, V. et al. A first-principles-based high fidelity, high throughput approach for the design of high entropy alloys. *Sci. Rep.* **12**, 11894 (2022).
39. Coury, F. G., Clarke, K. D., Kiminami, C. S., Kaufman, M. J. & Clarke, A. J. High throughput discovery and design of strong multicomponent metallic solid solutions. *Sci. Rep.* **8**, 8600 (2018).
40. Qi, J., Cheung, A. M. & Poon, S. J. High entropy alloys mined from binary phase diagrams. *Sci. Rep.* **9**, 15501 (2019).
41. Rittiruam, M. et al. High-throughput materials screening algorithm based on first-principles density functional theory and artificial neural network for high-entropy alloys. *Sci. Rep.* **12**, 16653 (2022).
42. Johnson, D. D., Singh, P., Smirnov, A. V. & Argibay, N. Universal maximum strength of solid metals and alloys. *Phys. Rev. Lett.* **130**, 166101 (2023).

43. Moorehead, M. et al. High-throughput synthesis of Mo–Nb–Ta–W high-entropy alloys via additive manufacturing. *Mater. Des.* **187**, 108358 (2020).

44. Melia, M. A. et al. High-throughput additive manufacturing and characterization of refractory high entropy alloys. *Appl. Mater. Today* **19**, 100560 (2020).

45. Ludwig, A., Zarnetta, R., Hamann, S., Savan, A. & Thienhaus, S. Development of multifunctional thin films using high-throughput experimentation methods. *Int. J. Mater. Res.* **99**, 1144–1149 (2008).

46. Zhou, Z. et al. Machine learning guided appraisal and exploration of phase design for high entropy alloys. *Npj Comput. Mater.* **5**, 1–9 (2019).

47. Johnson, D. D., Nicholson, D. M., Pinski, F. J., Gyorffy, B. L. & Stocks, G. M. Density-functional theory for random alloys: total energy within the coherent-potential approximation. *Phys. Rev. Lett.* **56**, 2088–2091 (1986).

48. Johnson, D. D. & Pinski, F. J. Inclusion of charge correlations in calculations of the energetics and electronic structure for random substitutional alloys. *Phys. Rev. B* **48**, 11553–11560 (1993).

49. Singh, P. et al. Martensitic transformation in FexMn80−xCo10Cr10 high-entropy alloy. *Phys. Rev. Lett.* **127**, 115704 (2021).

50. Khan, T. Z. et al. Towards stacking fault energy engineering in FCC high entropy alloys. *Acta Mater.* **224**, 117472 (2022).

51. Vegard, L. Die Konstitution der Mischkristalle und die Raumfüllung der Atome. *Z. Phys.* **5**, 17–26 (1921).

52. Inoue, A., Zhang, T. & Masumoto, T. Reductilization of embrittled La–Al–Ni amorphous alloys by viscous flow deformation in a supercooled liquid region. *J. Non-Cryst. Solids* **156–158**, 598–602 (1993).

53. Singh, P., Smirnov, A. V. & Johnson, D. D. Ta–Nb–Mo–W refractory high-entropy alloys: anomalous ordering behavior and its intriguing electronic origin. *Phys. Rev. Mater.* **2**, 055004 (2018).

54. Pugh, S. F. XCII Relations between the elastic moduli and the plastic properties of polycrystalline pure metals. *Lond. Edinb. Dublin Philos. Mag. J. Sci.* **45**, 823–843 (1954).

55. Thompson, R. P. & Clegg, W. J. Predicting whether a material is ductile or brittle. *Curr. Opin. Solid State Mater. Sci.* **22**, 100–108 (2018).

56. Vazquez, G. et al. Efficient machine-learning model for fast assessment of elastic properties of high-entropy alloys. *Acta Mater.* **232**, 117924 (2022).

57. Singh, P., Smirnov, A. V. & Johnson, D. D. Atomic short-range order and incipient long-range order in high-entropy alloys. *Phys. Rev. B* **91**, 224204 (2015).

58. Guo, S., Ng, C., Lu, J. & Liu, C. T. Effect of valence electron concentration on stability of fcc or bcc phase in high entropy alloys. *J. Appl. Phys.* **109**, 103505 (2011).

59. Sheikh, S. et al. Alloy design for intrinsically ductile refractory high-entropy alloys. *J. Appl. Phys.* **120**, 164902 (2016).

60. Senkov, O. N., Miracle, D. B. & Rao, S. I. Correlations to improve room temperature ductility of refractory complex concentrated alloys. *Mater. Sci. Eng. A* **820**, 141512 (2021).

61. Rahm, M., Zeng, T. & Hoffmann, R. Electronegativity seen as the ground-state average valence electron binding energy. *J. Am. Chem. Soc.* **141**, 342–351 (2019).

62. Senkov, O. N. & Miracle, D. B. Generalization of intrinsic ductile-to-brittle criteria by Pugh and Pettifor for materials with a cubic crystal structure. *Sci. Rep.* **11**, 4531 (2021).

63. Niu, H. et al. Extra-electron induced covalent strengthening and generalization of intrinsic ductile-to-brittle criterion. *Sci. Rep.* **2**, 718 (2012).

64. Wachtman, J. B., Tefft, W. E., Lam, D. G. & Apstein, C. S. Exponential temperature dependence of Young's modulus for several oxides. *Phys. Rev.* **122**, 1754–1759 (1961).

65. Steneteg, P. et al. Temperature dependence of TiN elastic constants from ab initio molecular dynamics simulations. *Phys. Rev. B* **87**, 094114 (2013).

66. Laplanche, G. et al. Temperature dependencies of the elastic moduli and thermal expansion coefficient of an equiatomic, single-phase CoCrFeMnNi high-entropy alloy. *J. Alloys Compd.* **623**, 348–353 (2015).

67. Arroyave, R., Shin, D. & Liu, Z.-K. Ab initio thermodynamic properties of stoichiometric phases in the Ni–Al system. *Acta Mater.* **53**, 1809–1819 (2005).

68. Hao, P. et al. Lattice constants from semilocal density functionals with zero-point phonon correction. *Phys. Rev. B* **85**, 014111 (2012).

69. Courtney, T. H. *Mechanical Behavior of Materials* 2nd edn (Waveland Press, 2005).

70. Senkov, O. N., Senkova, S. V. & Woodward, C. Effect of aluminum on the microstructure and properties of two refractory high-entropy alloys. *Acta Mater.* **68**, 214–228 (2014).

71. Guo, N. N. et al. Microstructure and mechanical properties of refractory MoNbHfZrTi high-entropy alloy. *Mater. Des.* **81**, 87–94 (2015).

72. Fazakas, É. et al. Experimental and theoretical study of Ti20Zr20Hf20Nb20X20 (X = V or Cr) refractory high-entropy alloys. *Int. J. Refract. Met. Hard Mater.* **47**, 131–138 (2014).

73. Senkov, O. N., Senkova, S. V., Miracle, D. B. & Woodward, C. Mechanical properties of low-density, refractory multi-principal element alloys of the Cr–Nb–Ti–V–Zr system. *Mater. Sci. Eng. A* **565**, 51–62 (2013).

74. Leclerc, N., Khosravani, A., Hashemi, S., Miracle, D. B. & Kalidindi, S. R. Correlation of measured load-displacement curves in small punch tests with tensile stress-strain curves. *Acta Mater.* **204**, 116501 (2021).

75. Su, R. et al. Enhanced oxidation resistance of (Mo95W5)85Ta10(TiZr)5 refractory multi-principal element alloy up to 1300 °C. *Acta Mater.* **215**, 117114 (2021).

76. Ouyang, G. et al. Oxidation resistance of a Mo–W–Si–B alloy at 1000–1300 °C: The effect of a multicomponent Mo–Si–B coating. *Appl. Surf. Sci.* **470**, 289–295 (2019).

77. Su, R. et al. Oxidation mechanism in a refractory multiple-principal-element alloy at high temperature. *Acta Mater.* **246**, 118719 (2023).

78. Maresca, F. & Curtin, W. A. Mechanistic origin of high strength in refractory BCC high entropy alloys up to 1900 K. *Acta Mater.* **182**, 235–249 (2020).

79. ASTM Standard B962-17, "*Standard Test Methods for Density of Compacted or Sintered Powder Metallurgy (PM) Products Using Archimedes' Principle,*" ASTM International, West Conshohocken, PA (2017).

80. ASTM Standard E9-09, "*Standard Test Methods of Compression Testing of Metallic Materials at Room Temperature,*" ASTM International, West Conshohocken, PA (2018)

81. Bruchhausen, M. et al. *European Standard on Small Punch Testing of Metallic Materials* (American Society of Mechanical Engineers Digital Collection, 2017)

82. Perdew, J. P., Burke, K. & Ernzerhof, M. Generalized gradient approximation made simple. *Phys. Rev. Lett.* **77**, 3865–3868 (1996).

ACKNOWLEDGEMENTS

AUTHOR CONTRIBUTIONS

G.O., J.C., M.J.K., and D.D.J. designed the project; J.C., M.J.K., D.D.J., and J.H.P. secured the funding; P.S. designed alloy selection criteria with D.D.J.; P.S. performed DFT calculations; P.S. and D.D.J. analyzed the DFT results; G.O., R.S., and O.S. performed experiments; G.O., R.S., J.C., M.J.K., O.S., J.H.P., D.M. analyzed the data. All authors contributed to the manuscript.

COMPETING INTERESTS

The authors declare no competing interests.

ADDITIONAL INFORMATION

Supplementary information The online version contains supplementary material available at https://doi.org/10.1038/s41524-023-01095-4.

Correspondence and requests for materials should be addressed to Gaoyuan Ouyang, Duane D. Johnson or Jun Cui.

Reprints and permission information is available at http://www.nature.com/reprints

Publisher's note Springer Nature remains neutral with regard to jurisdictional claims in published maps and institutional affiliations.